Submitted to

32nd International Conference on High Energy Physics, ICHEP04, August 16, 2004, Beijing
Abstract: **6-0177**
Parallel Session **6**

www-h1.desy.de/h1/www/publications/conf/conf_list.html

Dijets in Diffractive Photoproduction and Deep-Inelastic Scattering at HERA

H1 Collaboration

Abstract

Measurements are presented of differential dijet cross sections in low-$|t|$ diffractive photoproduction (photon virtuality $Q^2 < 0.01$ GeV^2) and deep-inelastic scattering processes (DIS, $Q^2 > 4$ GeV^2) of the type $ep \to eXY$, in which the photon dissociation system X is separated from a leading low-mass baryonic system Y by a large rapidity gap. The measurements are based on an integrated luminosity of 18 pb^{-1} and are performed in the same kinematic ranges besides Q^2. Dijet events are identified in the γp rest frame using the inclusive k_T cluster algorithm. The cross sections are given at the level of stable hadrons and correspond to the kinematic range $x_{I\!P} < 0.03$, $E_T^{*,\mathrm{jet1}} > 5$ GeV and $E_T^{*,\mathrm{jet2}} > 4$ GeV. The measurements of dijet rates in photoproduction and DIS are compared with NLO QCD predictions based on diffractive parton distributions previously obtained from a NLO QCD analysis of inclusive diffractive DIS. Whereas the diffractive dijet rate in DIS is in good agreement with QCD factorisation, the dijet rate in photoproduction is suppressed by about a factor 0.5 compared to the NLO QCD prediction. The results are suggestive of a breakdown of factorisation in photoproduction for both direct and resolved photon interactions. This is reminiscent of the observed breakdown of factorisation in diffractive dijet production in $p\bar{p}$ collisions.

1 Introduction

Quantum Chromodynamics (QCD) predicts that the cross section for diffractive deep-inelastic ep scattering (DDIS) factorises into universal diffractive parton densities (DPDFs) and process-dependent hard scattering coefficients [1] (QCD factorisation). Diffractive parton densities have been determined from DGLAP QCD fits to inclusive diffractive HERA data [2,3] and have been found to be dominated by the gluon distribution.

Final state configurations for which a partonic cross section is perturbatively calculable in QCD include dijet and heavy quark production, which are directly sensitive to the gluon component of the diffractive exchange. Previous measurements of diffractive dijet and D^* meson production in DIS have been found to be described by next-to-leading order (NLO) QCD calculations using DPDFs and assuming QCD factorisation [4].

However, applying this approach in leading order (LO) QCD calculations to predict diffractive dijet production in $p\bar{p}$ collisions at the Tevatron leads to an overestimation of the observed rate by approximately one order of magnitude [5]. This discrepancy has been attributed to the presence of the additional beam hadron remnant in $p\bar{p}$ collisions, which leads to secondary interactions and a breakdown of factorisation. The suppression, often characterised by a reduced 'rapidity gap survival probability,' cannot be calculated perturbatively and has been parameterised in various ways (see, e.g., [6]).

The transition from DIS to hadron-hadron scattering can be studied at HERA in a comparison of scattering processes in DIS and in photoproduction. In photoproduction, the beam lepton emits a quasi-real photon which interacts with the proton (γp collision). Processes in which a real photon participates directly in the hard scattering are expected to be similar to the deep-inelastic scattering of highly virtual photons ("point-like photon"). In contrast, processes in which the photon is first resolved into partons which then initiate the hard scattering resemble hadron-hadron scattering. Via resolved photon processes in hard photoproduction, parton final states are accessible, which are present in the equivalent $p\bar{p}$ collisions but not in DIS. Different prescriptions for diffraction can therefore be tested in the regime of hard diffractive DIS and photoproduction.

In this paper, measurements of diffractive dijet cross sections in DIS and photoproduction are presented, based on data collected with the H1 detector at HERA. For photoproduction the integrated luminosity is increased by one order of magnitude with respect to previous results [7]. Jets are defined using the inclusive k_T cluster algorithm with asymmetric cuts on the jet transverse energies to facilitate comparisons with NLO predictions. Apart from the different ranges for the photon virtuality, the two measurements are performed in the same kinematic ranges to allow the closest possible comparison of the cross sections. The cross sections are compared with NLO QCD predictions based on DPDFs.

2 Kinematics

The generic diffractive electron-proton interaction $ep \rightarrow eXY$ is illustrated in Figure 1. The electron[1] (4-momentum k) exchanges a photon (q) which interacts with the proton (P). The

[1]Throughout the paper, the word 'electron' is used synonymously for positrons.

final state hadrons produced are, by definition, divided into the systems X and Y, separated by the largest gap in the hadron rapidity distribution. The system Y lies in the outgoing proton beam direction.

Examples of hard diffractive processes leading to jets in the final state at HERA are given by the diagrams of Figure 2 for the photon-gluon fusion production mechanism ("direct" or "point-like" photon process) and a process in which the photon develops hadronic structure from which a single parton undergoes the hard scatter ("resolved" or "hadron-like" photon process). In photoproduction, the latter process contributes significantly, whereas in DIS it is suppressed due to the large photon virtuality.

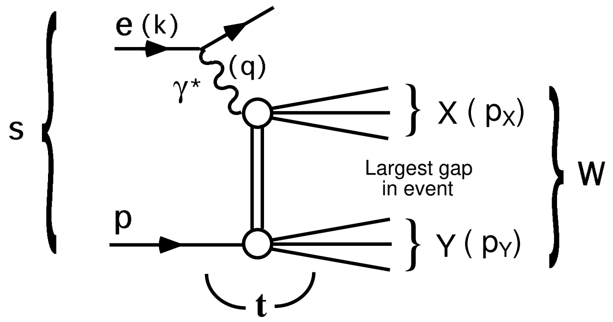

Figure 1: Illustration of the generic diffractive process $ep \to eXY$. The systems X and Y are separated by the largest gap in the rapidity distribution of the final state hadrons.

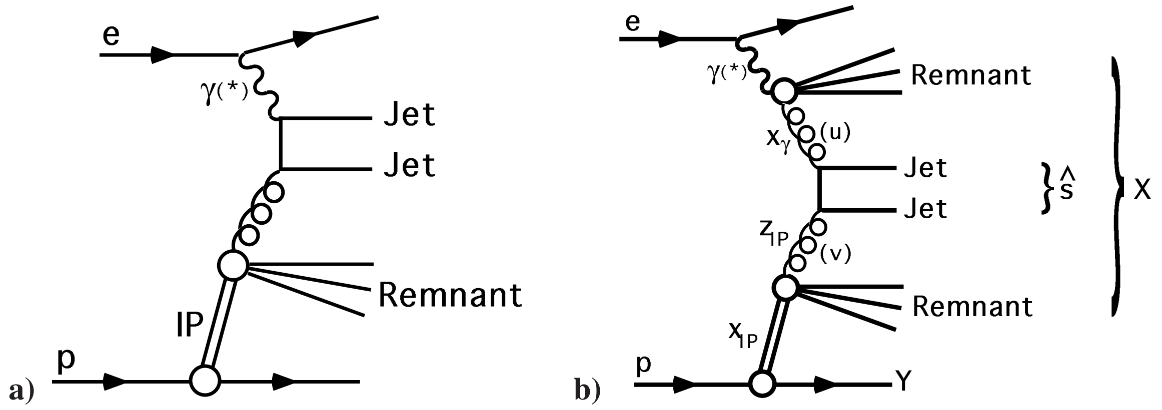

Figure 2: Leading order diagrams for diffractive dijet production at HERA. a) Direct (point-like) photon process (photon-gluon fusion), b) resolved (hadron-like) photon process.

The following kinematic variables are defined:

$$s \equiv (k+P)^2; \qquad Q^2 \equiv -q^2; \qquad y \equiv \frac{q \cdot P}{k \cdot P}. \tag{1}$$

The variable y is related to the γp centre-of-mass energy W by $W = \sqrt{y\,s - Q^2}$. With p_X and

p_Y representing the 4-momenta of the systems X and Y, the data are discussed in terms of

$$M_X^2 \equiv p_X^2; \quad M_Y^2 \equiv p_Y^2; \quad t \equiv (P - p_Y)^2; \quad x_{I\!P} \equiv \frac{q \cdot (P - p_Y)}{q \cdot P}. \tag{2}$$

The quantities M_X and M_Y are the invariant masses of the systems X and Y, t is the squared 4-momentum transferred between the incoming proton and the photon, and $x_{I\!P}$ is the fraction of the proton beam momentum transferred to the system X. With u and v denoting the 4-momenta of the partons entering the hard subprocess from the photon and the proton, respectively (as indicated in Figure 2b, for the direct process $u = q$), the dijet system has squared invariant mass

$$\hat{s} = M_{12}^2 = (u + v)^2. \tag{3}$$

The longitudinal fractional momenta carried by the partons from the photon (x_γ) and the diffractive exchange ($z_{I\!P}$) are given by

$$x_\gamma = \frac{P \cdot u}{P \cdot q}; \qquad z_{I\!P} = \frac{q \cdot v}{q \cdot (P - p_Y)}. \tag{4}$$

The measurements are performed in the region of small $x_{I\!P}$, large t, and small masses M_Y, where the cross section is dominated by diffractive scattering in which the proton remains intact.

3 Diffractive Parton Densities

3.1 QCD Factorisation in Diffractive ep Collisions

QCD predicts that in the leading $\log(Q^2)$ approximation the cross section for the diffractive process $\gamma^* p \to Xp$ factorises into universal diffractive parton distributions of the proton convoluted with process-dependent hard scattering coefficients [1]. The DPDFs [8–10] represent probability distributions for a parton in the proton under the constraint that the proton remains intact with particular values of t and $x_{I\!P}$. At leading twist,

$$\frac{\mathrm{d}^2\sigma(x, Q^2, x_{I\!P}, t)^{\gamma^* p \to pX}}{\mathrm{d}x_{I\!P}\,\mathrm{d}t} = \sum_i \int_x^{x_{I\!P}} \mathrm{d}\xi\; \hat{\sigma}^{\gamma^* i}(x, Q^2, \xi)\; p_i^D(\xi, Q^2, x_{I\!P}, t)\;. \tag{5}$$

The factorisation formula is valid for large enough Q^2 and at fixed $x_{I\!P}$ and t. It also applies to the case of proton dissociation into a system of fixed small mass M_Y. The partonic cross sections $\hat{\sigma}^{\gamma^* i}$ are the same as for inclusive DIS and the diffractive parton distributions p_i^D, which are not known from first principles, should obey the DGLAP evolution equations. Analogously to inclusive DIS, the diffractive parton distributions can be determined from measurements by a DGLAP QCD fit to the inclusive diffractive DIS cross section. First analyses of this kind were performed in [2, 11, 12] based on measurements of the diffractive structure function F_2^D at HERA. The test of the QCD factorisation concept in diffractive dijet production in DIS and photoproduction is the goal of this paper.

3.2 H1 Diffractive Parton Densities

Diffractive parton distributions of the proton have been determined through DGLAP QCD fits to inclusive diffractive DIS measurements by the H1 collaboration in [2,3]. The fits were made under the additional assumptions that the $x_{I\!P}, t$ dependence of the parton distributions factorises from the x, Q^2 dependence:

$$p_i^D(x_{I\!P}, t, x, Q^2) = f_{I\!P/p}(x_{I\!P}, t) \;\; p_{i,I\!P}(\beta = x/x_{I\!P}, Q^2). \tag{6}$$

This so-called *Regge* factorisation assumption, in the literature often referred to as the *resolved pomeron* model [13], implies that the diffractive exchange can be treated as a quasi-real object with a partonic structure, given by parton distributions $p_{i,I\!P}(\beta, Q^2)$. The variable β then corresponds to the longitudinal momentum fraction of the diffractive exchange carried by the struck parton in the *pomeron*. The first term $f_{I\!P/p}(x_{I\!P}, t)$ (also called the *pomeron flux factor*) represents the probability for scattering off a pomeron with particular values of $x_{I\!P}$ and t. It should be stressed that no proof in QCD exists for the assumption of Eq. (6). At the present level of experimental precision the assumption is consistent with inclusive diffractive H1 measurements for $x_{I\!P} < 0.01$. At larger $x_{I\!P}$ a contribution from sub-leading meson ("reggeon") exchange has to be taken into account, such that the diffractive PDFs, integrated over t, are given by:

$$p_i^D(x_{I\!P}, \beta, Q^2) = f_{I\!P/p}(x_{I\!P})\, p_{i,I\!P}(\beta, Q^2) + f_{I\!R/p}(x_{I\!P})\, p_{i,I\!R}(\beta, Q^2). \tag{7}$$

The pomeron and reggeon flux factors are given by

$$f_{\{I\!P,I\!R\}/p}(x_{I\!P}) = \int_{t_{\rm cut}}^{t_{\rm max}} \frac{e^{B_{\{I\!P,I\!R\}}t}}{x_{I\!P}^{2\alpha_{\{I\!P,I\!R\}}(t)-1}}\, {\rm d}t, \tag{8}$$

where $t_{\rm cut} = -1.0$ GeV^2, $t_{\rm max}$ is the maximum kinematically allowed value of t and the pomeron and reggeon trajectories are assumed to be linear functions of t:

$$\alpha_{\{I\!P,I\!R\}}(t) = \alpha_{\{I\!P,I\!R\}}(0) + \alpha'_{\{I\!P,I\!R\}}t. \tag{9}$$

The latest DGLAP QCD fits to the most recent available inclusive DDIS measurements were presented by the H1 Collaboration in [3]. The pomeron parton distributions are composed of a light flavour singlet and a gluon distribution, which are evolved using the DGLAP equations, both in leading and in next-to-leading order. The strong coupling constant α_s was fixed by setting $\Lambda_{\rm QCD}^{\overline{\rm MS}} = 0.2$ GeV for 4 flavours, using the 1-loop and 2-loop expressions for α_s at LO and NLO, respectively. The charm mass is set to $m_c = 1.5$ GeV. Pion PDFs are used for the meson. The result of the fit is shown in Fig. 3. The uncertainty shown for the NLO PDFs includes the experimental uncertainty arising from the errors of the fitted data as well as the theoretical uncertainty, estimated by variations of m_c, $\Lambda_{\rm QCD}$ and the parameters used in the pomeron and reggeon flux factors. The total uncertainty of the NLO gluon distribution is $\approx 30\%$ at a parton fractional momentum $z_{I\!P} \approx 0.5$ and increases to more than 50% for $z_{I\!P} \gtrsim 0.7$. These parton densities are referred to as 'H1 2002 fit' in the present paper and they are used for the comparison of the measured cross sections with QCD predictions. The earlier 'H1 fit 2' PDFs [2] are used for detector unsmearing.

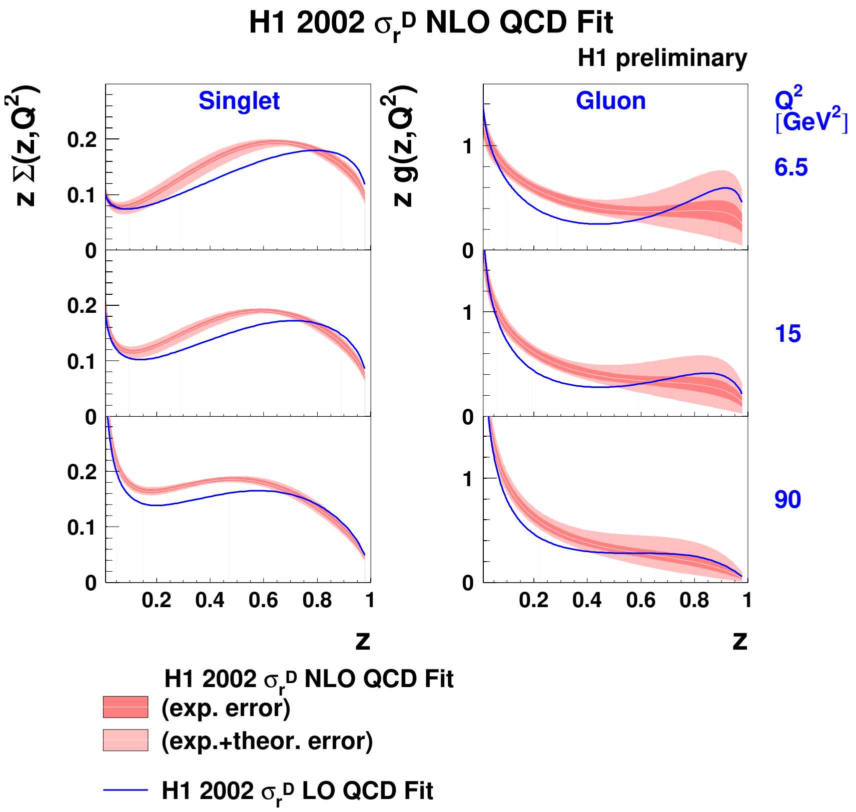

Figure 3: Quark singlet (left) and gluon (right) distribution functions at LO (lines) and NLO (bands) of the diffractive exchange at several values of Q^2, obtained from DGLAP QCD analyses of inclusive diffractive DIS data (from [3]).

3.3 Diffractive Dijet Production

The diffractive parton densities can be used to predict diffractive final state cross sections, such as dijet production in DIS and photoproduction. In these predictions the jet transverse momentum is used for the renormalisation and factorisation scales. It has been demonstrated in [14] that diffractive dijet production in DIS is described to within 10% by the parton distributions corresponding to 'H1 fit 2.' The 'H1 fit 2' parton densities have also been used to predict diffractive dijet production in $p\bar{p}$ collisions at the Tevatron. There, the measured diffractive structure function of the anti-proton is overestimated by approximately one order of magnitude [5]. For the recent 'H1 2002 fit' DPDFs, this discrepancy diminishes slightly but is still approximately a factor 7 [3]. In the present paper, diffractive dijet production in DIS and photoproduction are compared with calculations based on the recent 'H1 2002 fit' DPDFs.

4 Monte Carlo Simulations

In the analyses, different Monte Carlo programs are used to correct the measured distributions for detector inefficiencies and smearing. The program RAPGAP 2.08 [15] is used to obtain predictions based on LO H1 diffractive parton densities convoluted with LO matrix elements for the hard QCD $2 \to 2$ subprocess. The appropriate partonic cross sections are also convoluted with the parton densities of the photon. In photoproduction the leading order GRV '94 parton distribution functions [16] are used for the resolved photon component. These parton densities were found to give a good description of the effective photon structure function as measured by H1 [17]. For DIS, processes with a resolved virtual photon are generated in which the structure of the photon is given by the SAS-2D parameterisation [18], which gives a reasonable description of inclusive dijet production in a similar Q^2 range [19]. The PDFs are taken at the scale $\mu^2 = \hat{p}_T^2 + 4m_{q\bar{q}}^2$, where $\hat{p}_T$ is the transverse momentum of the emerging hard partons and $m_{q\bar{q}}$ is the invariant mass of the produced quark pair.

To correct the measured distributions for detector smearing the 'H1 fit 2' DPDFs are used. To avoid divergences in the calculation of the matrix elements, a cut $\hat{p}_T > 3$ GeV is applied at the generator level for DIS and $\hat{p}_T > 2$ GeV for photoproduction. No significant losses result from these cuts for the selected jets with $E_T^{*,\mathrm{jet1}} > 5$ GeV and $E_T^{*,\mathrm{jet2}} > 4$ GeV. Higher order effects are simulated using parton showers [20] in the leading log(μ) approximation (MEPS), and the Lund string model [21] is used for hadronisation. RAPGAP does not include any factorisation breaking effects due to remnant interactions. Photon radiation from the electron lines is simulated using the program HERACLES [22]. The PYTHIA 6.1 Monte Carlo program [23] is used to simulate inclusive dijet photoproduction processes to evaluate migrations from high M_Y and high $x_{I\!P}$. For the corresponding correction in DIS, the RAPGAP program is used in inclusive DIS mode.

5 Next-to-leading Order QCD Calculations

QCD factorisation in diffractive DIS [1] implies that the hard scattering cross section for the interaction of the virtual photon with a parton from the DPDFs is identical to the non-diffractive case. Therefore, programs which calculate fixed order partonic cross sections for dijet production in ordinary DIS and photoproduction can also be used in the case of diffraction.

To calculate diffractive dijet cross sections to NLO in QCD for deep-inelastic electron-proton scattering, the DISENT [24] program is used, as suggested in [25]. It was demonstrated in [26] that calculations using this program agree very well with the results from other programs. To obtain NLO cross sections for diffractive dijet photoproduction, the program by Frixione et al. [27] is used. Both programs are interfaced to the NLO diffractive parton distributions obtained in [3]. For the Frixione calculation, the GRV HO photon PDFs [16] are used for the hadronic component of the photon.

The NLO programs are adapted to calculate diffractive cross sections as follows. The cross section at a fixed value of $x_{I\!P}$ and $t = 0$ is calculated by reducing the nominal proton beam energy by a factor $x_{I\!P}$. Since the $x_{I\!P}$ and t dependences of the diffractive PDFs factorise from the β and Q^2 dependences, the proton PDFs can be replaced by the PDFs of the diffractive exchange $p_{i,I\!P}(\beta, Q^2)$. The calculated cross sections are multiplied by the t-integrated flux factor $f_{I\!P/p}(x_{I\!P}) = \int \mathrm{d}t\, f_{I\!P/p}(x_{I\!P}, t)$. The same prescription is applied to calculate the contribution from meson exchange using pion PDFs and the flux factor $f_{I\!R/p}(x_{I\!P})$. The partonic configurations are calculated for $t = 0$, such that kinematic effects of a finite value of t are neglected.

Since the measured cross sections correspond to an interval in $x_{I\!P}$, the integration over $x_{I\!P}$ is approximated by integrating the results obtained for a set of suitably chosen $x_{I\!P}$ points ("$x_{I\!P}$ slicing"). The number of $x_{I\!P}$ points is chosen to ensure the calculation is of sufficient precision.

For the (N)LO calculations, the diffractive parton distributions are used in their respective version. The strong coupling constant α_s is set to the value assumed in the QCD fit from which the PDFs were extracted, using the corresponding 1(2)-loop expression and taking $\Lambda_{QCD}^{\overline{MS}} = 0.2$ GeV for 4 flavours. The parton configurations resulting from the calculations are subjected to the same jet algorithm as is used for the measured cross sections. The renormalisation scale is set to the transverse energy of the leading jet in the photon-proton centre-of-mass frame: $\mu_r = E_T^{*,\mathrm{jet1}}$. For DISENT, the factorisation scale is set to $\mu_f = 6.2$ GeV, corresponding to the average E_T of the leading jet observed in the DIS measurement. For the Frixione calculation, the factorisation scale is set to be equal to the renormalisation scale.

Since the calculations refer to jets of partons, whereas the measurements refer to jets of hadrons, the calculated NLO cross sections have to be corrected for the effects of hadronisation. In the case of diffraction, these also influence the diffractive kinematics, which are defined on the basis of the largest gap in rapidity in the hadronic final state. The hadronisation corrections, defined as

$$1 + \delta_{\mathrm{had}} = \frac{\sigma_{\mathrm{dijet}}^{\mathrm{hadron}}}{\sigma_{\mathrm{dijet}}^{\mathrm{parton}}} \;, \qquad (10)$$

are determined using the Monte Carlo generator RAPGAP with parton showers enabled to simulate higher orders. The parton level cross section is defined in the same way as for the NLO calculation and is obtained using the same jet algorithm and the same definitions of the kinematic variables. Lund string fragmentation is used for hadronisation. The size of the hadronisation corrections in DIS is of the order of a few percent on average, reaching 20% in certain regions of the phase space. The size of the correction decreases with increasing p_T of the jets. In photoproduction, the correction lowers the parton level cross section by ≈ 10 % on average. The correction is particularly large in the second highest bin of the x_γ^{jets} distribution in which resolved photon interactions dominate. Here, events for which $x_\gamma^{\mathrm{jets}} \approx 1$ at the parton level are smeared towards lower values due to hadronisation. Uncertainties on the hadronisation corrections have not yet been estimated for the results in this paper.

6 Experimental Procedure

6.1 H1 Detector

A detailed description of the H1 detector can be found in [28]. Here, a brief account of the components most relevant to the present analyses is given. The H1 coordinate system convention defines the outgoing proton beam direction as the positive z axis and the polar scattering angle θ is measured relative to this axis such that the pseudorapidity $\eta = -\ln\tan(\theta/2)$ increases with z.

The hadronic final state X is measured by combining information from a tracking and a calorimeter system. The central ep interaction region is surrounded by two large concentric drift chambers, located inside a 1.15 T solenoidal magnetic field. Charged particle momenta are measured in the range $-1.5 < \eta < 1.5$ with a resolution of $\sigma(p_T)/p_T \simeq 0.01\, p_T/$GeV. A finely segmented electromagnetic and hadronic liquid argon calorimeter (LAr) covers the range $-1.5 < \eta < 3.4$. The energy resolution is $\sigma(E)/E \simeq 0.11/\sqrt{E/\mathrm{GeV}}$ for electromagnetic showers and $\sigma(E)/E \simeq 0.50/\sqrt{E/\mathrm{GeV}}$ for hadrons, as measured in test beams. The backward region $-4 < \eta < -1.4$ is covered by a lead/scintillating fibre calorimeter (SPACAL, [29]) which is used to identify and measure the scattered electron in DIS events.

The forward region is covered by the Forward Muon Detector (FMD) and the Proton Remnant Tagger (PRT). The 3 pre-toroid double layers of drift chambers of the FMD are used to detect particles directly in the region $1.9 < \eta < 3.7$, and from larger pseudorapidities via beam-pipe scattering. The PRT consists of a set of scintillators surrounding the beam pipe at $z = 26$ m and covers the region $6 < \eta < 7.5$.

The ep luminosity is measured via the Bethe-Heitler Bremsstrahlung process $ep \rightarrow ep\gamma$, the final state electron and photon being detected in crystal calorimeters at $z = -33$ m (small angle electron detector) and $z = -103$ m (photon detector), respectively. The small angle electron detector is also used to tag and measure the scattered electron in photoproduction.

6.2 Event Selection

The data used in these analyses were taken in the 1996 and 1997 running periods, in which HERA collided 820 GeV protons with 27.5 GeV positrons. The photoproduction data are collected using a trigger which requires the scattered electron to be measured in the small angle electron detector, at least 3 tracks in the central jet chamber and an event vertex. A veto cut requiring less than 2 GeV of energy deposited in the photon detector suppresses accidental coincidences with Bremsstrahlung events. DIS events are collected using a trigger which requires the scattered electron to be detected in the backward electromagnetic calorimeter (SPACAL) with an energy of at least 6.5 GeV, an event vertex and at least one large transverse momentum track in the central region of the detector.

Rapidity gap events are selected by requiring an absence of activity in the forward direction. No signals above noise levels are allowed in the FMD and PRT. In the LAr, no cluster with an energy of more than 400 MeV is allowed in the region $\eta > 3.2$. These selection criteria ensure that the gap between the systems X and Y spans at least the region $3.2 < \eta < 7.5$, and that $M_Y < 1.6$ GeV and $-t < 1$ GeV^2. A cut $x_{I\!P} < 0.03$ further reduces non-diffractive contributions.

Jets are formed from the tracks and clusters of the hadronic final state X, using the inclusive k_T cluster algorithm [30] with a distance parameter of 1.0 in the γp rest frame, which for photoproduction is identical to the laboratory frame up to a Lorentz boost along the beam axis. At least two jets are required, with transverse energies $E_T^{*,\mathrm{jet1}} > 5$ GeV and $E_T^{*,\mathrm{jet2}} > 4$ GeV for the leading and subleading jet, respectively.[2] The jet axes of the two leading jets are required to lie within the region $-1 < \eta_{\mathrm{jet}}^{\mathrm{lab}} < 2$, well within the acceptance of the LAr calorimeter.

[2]The '*' denotes variables in the γp system.

6.3 Kinematic Reconstruction

The hadronic system X, which contains the jets, is measured in the LAr and SPACAL calorimeters and the central tracking system. Calorimeter cluster energies and track momenta are combined using algorithms which avoid double counting [31].

Cross sections are measured differentially in the invariant mass M_{12} of the dijet system, the transverse momentum of the leading jet $p_T^{*,\mathrm{jet1}}$ and the mean pseudorapidity $\langle \eta_{\mathrm{jet}}^{\mathrm{lab}} \rangle$ of the two jets in the laboratory frame. The jet separation $\left|\Delta\eta_{\mathrm{jet}}^{*}\right|$ is reconstructed in the γp rest frame where it is related to the scattering angle of the hard subprocess.

6.3.1 Reconstruction of Photoproduction Events

In the photoproduction analysis, the energy E_e' of the scattered electron is measured in the small scattering angle electron detector and y is reconstructed according to

$$y = 1 - E_e'/E_e, \tag{11}$$

where E_e is the electron beam energy. The geometrical acceptance of the detector limits the measurement to $Q^2 < 0.01$ GeV^2 and $0.3 < y < 0.65$.

The estimators x_γ^{jets} and $z_{I\!P}^{\mathrm{jets}}$ of the fractional momenta of the partons entering the hard subprocess are reconstructed as:

$$x_\gamma^{\mathrm{jets}} = \frac{\sum_{\mathrm{jets}} (E - p_z)}{2\, y\, E_e}; \qquad z_{I\!P}^{\mathrm{jets}} = \frac{\sum_{\mathrm{jets}} (E + p_z)}{2\, x_{I\!P}\, E_p}, \tag{12}$$

where the sum runs over the two jets comprising the dijet system and E_p is the proton beam energy. The invariant mass of the hadronic system M_X is reconstructed according to

$$M_X = \sqrt{\frac{M_{12}^2}{z_{I\!P}^{\mathrm{jets}}\; x_\gamma^{\mathrm{jets}}}}. \tag{13}$$

The variable $x_{I\!P}$ is reconstructed according to

$$x_{I\!P} = \frac{\sum_X (E + p_z)}{2\, E_p}, \tag{14}$$

where the sum runs over all objects in the X system.

6.3.2 Reconstruction of DIS Events

In DIS, E_e' is measured in the backward calorimeter SPACAL and y and Q^2 are reconstructed using in addition the electron scattering angle θ according to

$$y = 1 - \frac{E_e'}{E_e} \sin^2 \frac{\theta_e}{2}, \quad Q^2 = 4 E_e E_e' \cos^2 \frac{\theta_e}{2}. \tag{15}$$

Kinematic ranges of cross sections

Photoproduction	DIS
$Q^2 < 0.01$ GeV^2	$4 < Q^2 < 80$ GeV^2
$165 < W < 242$ GeV	
inclusive k_T jet algorithm, distance parameter=1	
$N_{\text{jet}} \geq 2$	
$E_T^{*,\text{jet1}} > 5$ GeV	
$E_T^{*,\text{jet2}} > 4$ GeV	
$-1 < \eta^{\text{lab}}_{\text{jet}(1,2)} < 2$	$-3 < \eta^{*}_{\text{jet}(1,2)} < 0$
$x_{I\!P} < 0.03$	
$M_Y < 1.6$ GeV	
$-t < 1$ GeV^2	

Table 1: The kinematic ranges defining the measured cross sections.

The quantity M_X is reconstructed from the sum of all observed energy deposits above noise levels, excluding the scattered electron:

$$M_X^2 = (\sum_i E_i)^2 - (\sum_i \vec{p_i})^2. \tag{16}$$

The variable $x_{I\!P}$ is reconstructed according to

$$x_{I\!P} = \frac{Q^2 + M_X^2}{Q^2 + W^2}. \tag{17}$$

The estimators x_γ^{jets} and $z_{I\!P}^{\text{jets}}$ are reconstructed as

$$x_\gamma^{\text{jets}} = \frac{\sum_{\text{jets}} (E - p_z)^*}{\sum_{\text{X}} (E - p_z)^*}, \qquad z_{I\!P}^{\text{jets}} = \frac{Q^2 + M_{12}^2}{Q^2 + M_X^2}. \tag{18}$$

6.4 Cross Section Measurement

The measured cross sections are defined at the level of stable hadrons. The data are corrected for detector inefficiencies and migrations of kinematic quantities in the reconstruction using the RAPGAP Monte Carlo program. For generated events, the H1 detector response is simulated in detail and the Monte Carlo events are subjected to the same analysis chain as the data. The simulation gives a good description of the shapes of all data distributions. According to the simulations, the detector level observables are well correlated with the hadron level quantities.

The kinematic regions in which the cross sections are measured are given in Table 1. For the DIS measurement, the pseudorapidity range $-3 < \eta^* < 0$ in the γp frame corresponds approximately to the range $-1 < \eta < 2$ in the laboratory frame.

Migrations from large M_Y and $x_{I\!P}$ are corrected for using PYTHIA for photoproduction and RAPGAP for DIS. The net smearing about the measurement boundary $M_Y = 1.6$ GeV is evaluated with the DIFFVM [32] simulation of proton dissociation.

An analysis of systematic uncertainties has been performed in which the sensitivity of the measurements to variations of the detector calibration and the Monte Carlo models used for acceptance and migration corrections are evaluated. The dominant systematic error for the photoproduction analysis arises from the uncertainty in the LAr calorimeter energy scale and the migrations about $M_Y = 1.6$ GeV. For the DIS measurement, the dominant uncertainty arises from the acceptance and migration corrections.

7 Results

Comparisons at leading and next-to-leading order of the QCD calculations based on the diffractive parton distributions obtained from QCD fits to inclusive diffractive DIS data [3], with the measured dijet production cross sections in diffractive DIS and photoproduction are presented in Figs. 4–10. The inner vertical error bars represent the statistical errors and the outer error bars denote the quadratic sum of the statistical and uncorrelated systematic errors. The shaded band around the data points indicates the correlated normalisation uncertainties of the measurements.

7.1 Diffractive Dijet Production in DIS

In Figure 4a, the differential cross section for dijet production in diffractive DIS is presented as a function of $z_{I\!P}^{\rm jets}$, an estimator of the longitudinal momentum fraction of the diffractive exchange entering the hard scattering. The measurement is compared with NLO calculations obtained with the DISENT program interfaced to the 'H1 2002 fit' diffractive PDFs. The prediction is corrected for hadronisation effects. The band around the NLO calculation indicates the uncertainty arising from variations of the renormalisation scale by factors 0.5 and 2. The uncertainty is ≈ 20 % on average. The variation of the factorisation scale by factors 0.5 and 2 results in a change of the cross section by $\pm 10\%$ on average. This factorisation scale uncertainty is not included in the NLO band. The uncertainty of the NLO calculation does not yet include the uncertainty in the diffractive PDFs and the uncertainty arising due to the imperfect knowledge of the hadronisation corrections. The NLO prediction is in good agreement with the measurement at $z_{I\!P}^{\rm jets} < 0.6$. At higher values the prediction overestimates the cross section. Within the additional PDF uncertainty the calculation is compatible with the measurement.

The cross section is shown as a function of $\log_{10}(x_{I\!P})$ in Figure 4b. It is well described within the uncertainties by the NLO calculation. The cross section differential in the jet variables $p_T^{*,\rm jet1}$, $\langle \eta_{\rm jet}^{\rm lab} \rangle$, $\left|\Delta\eta_{\rm jet}^{*}\right|$ and M_{12} is shown in Figure 5. Also shown are the DISENT predictions at NLO with and without hadronisation corrections and at LO without hadronisation corrections. The NLO corrections to the LO cross section amount to a factor ≈ 1.9 on average. The NLO correction decreases smoothly with increasing $p_T^{*,\rm jet1}$ to 1.5 for $p_T^{*,\rm jet1} > 9$ GeV. The NLO calculation is in good agreement with the measured distributions. For $\eta_{\rm jet}^{\rm lab} < -0.4$

the prediction overestimates the cross section. This is kinematically related to the excess observed at high $x_\gamma^{\rm jets}$ which is shown in Figure 6d. The cross section is shown in Figure 6a–c as function of Q^2, y and M_X. Good agreement between the measurements and the calculations is found for these variables. The concept of QCD factorisation is compatible with the measured diffractive DIS dijet cross section. Similar results have been found in a previous diffractive dijet analysis [4] and in [33] for diffractive heavy quark production at HERA.

Also shown in Figure 4 is the prediction of the LO Monte Carlo event generator RAPGAP with parton showers included as a model for higher order corrections. The prediction is lower by $\approx 20\%$ compared with the NLO calculation and is in reasonable agreement with the measured distribution within the uncertainties.

7.2 Diffractive Photoproduction of Dijets

The cross section for diffractive dijet photoproduction is presented in Figure 7a as a function of $z_{I\!P}^{\rm jets}$. The measurement is compared with NLO predictions obtained with the Frixione et al. program interfaced to the NLO 'H1 2002 fit' diffractive PDFs and the NLO GRV photon PDFs. The calculation is corrected for hadronisation effects. The uncertainty shown on the NLO calculation results from simultaneous variations of the renormalisation and factorisation scales by factors 0.5 and 2. The uncertainty of the NLO calculation does not yet include the uncertainty in the diffractive PDFs and the uncertainty arising from the imperfect knowledge of the hadronisation corrections. The NLO prediction overestimates the cross section by a factor ≈ 2. This is seen also in Figure 7b where the cross section is shown as a function of $x_\gamma^{\rm jets}$. The same measured cross sections as a function of $z_{I\!P}^{\rm jets}$ and $x_\gamma^{\rm jets}$ are shown in Figure 8a and 8b, respectively, where an overall normalisation factor 0.5 has been applied to the NLO prediction. With this additional suppression factor for both the hadron-like and the point-like components, good agreement is obtained with the measurements except at large $z_{I\!P}^{\rm jets}$. The calculation is compatible with the measured cross section also at large $z_{I\!P}^{\rm jets}$ when the uncertainties due to the diffractive PDFs are taken into account.

The cross section is shown as a function of $\log_{10}(x_{I\!P})$ and y in Figure 8c and 8d, respectively. The scaled NLO prediction describes the measured distributions well within the experimental uncertainties. In Figure 9 the cross section is shown as a function of the jet variables $p_T^{\rm jet1}$, $\langle\eta_{\rm jet}^{\rm lab}\rangle$, $|\Delta\eta_{\rm jet}|$ and M_{12}. The NLO prediction with the additional scaling factor 0.5 describes the cross section well within the experimental and theoretical uncertainties. All measured distributions can be well described if a suppression factor of 0.5 is applied which suppresses both the direct and the resolved components.

In the following, the effect of a suppression of only those processes with a significant photon remnant energy is investigated. This is suggested by models which attribute factorisation breaking to secondary interactions among spectators. A suppression factor 0.34 is applied to that part of the photoproduction NLO calculation for which at the parton level $x_\gamma^{\rm jets} < 0.9$. The factor 0.34 has been calculated in [34] as a relative suppression for resolved photoproduction when the ratios of diffractive to inclusive jet production are compared in DIS and photoproduction. The result is shown in Figure 10, where the cross section is displayed as a function of $x_\gamma^{\rm jets}$ and y. The cut $x_\gamma^{\rm jets} < 0.9$ has been varied between 0.85 and 0.95. For the $x_\gamma^{\rm jets}$ distribution this leads to changes of the prediction in the highest $x_\gamma^{\rm jets}$ bin of $\pm 10\%$. This model cannot describe the shapes of the cross section as a function of $x_\gamma^{\rm jets}$ and y.

Also shown in Figure 7 is the prediction of the LO Monte Carlo program RAPGAP with parton showers included as a model for higher order corrections. The RAPGAP prediction uses the LO versions of the diffractive PDFs and the photon PDFs. It is in good agreement with the measurement. In contrast to the situation in DIS where the parton shower cascade significantly increases the cross section, the leading order parton level dijet cross section in photoproduction is reduced by the inclusion of parton showers.

7.3 Ratio of Dijet Cross Sections in Diffractive Photoproduction and DIS

In Figure 11 the ratio of the measured cross section to that predicted by the NLO calculation is shown as a function of the inelasticity variable y in the DIS and photoproduction kinematic regions. The shown y range corresponds to a range of $165 < W < 242$ GeV for the γp centre-of-mass energy W. The NLO calculations are based on the 'H1 2002 fit' diffractive parton densities and are corrected for hadronisation. The vertical error bars correspond to the quadratic sum of the statistical errors and the systematic errors of the data which are uncorrelated among the y bins. The error band around the ratio points specify the normalisation uncertainty on the measurements which is correlated among the bins. Shown at the bottom of the figure is the uncertainty on the ratio resulting from the variation of the renormalisation scale μ_r in the DIS NLO calculation between $0.5 < \mu_r/E_T^{*,\rm jet1} < 2$. The scale dependence is similar for the NLO calculation in photoproduction. If the same scale is used for DIS and photoproduction the scale uncertainty is largely correlated between the two kinematic ranges. Not included is the uncertainty resulting from the uncertainty on the diffractive parton densities and the uncertainty due to the imperfect knowledge of the hadronisation corrections.

The ratio of data to NLO prediction for DIS is compatible with unity within the experimental uncertainties throughout the measured y range. The ratio for photoproduction is around 0.5 throughout the y range indicating a suppression factor which is independent of the centre-of-mass energy within the uncertainties. Integrated over the measured kinematic range the ratio of data to NLO expectation for photoproduction is a factor 0.5 ± 0.1 (exp.) smaller than the same ratio in DIS. The uncertainty is estimated by adding the total experimental errors of both measurements in quadrature and does not include uncertainties in the calculations. This factor indicates a breaking of QCD factorisation in diffractive dijet photoproduction. The suppression factor found in photoproduction has to be compared with the factor $\approx 1/7$ needed to account for the suppression in single-diffractive dijet production at the Tevatron [3, 5].

From a comparison of the LO RAPGAP prediction with the cross sections in DIS and photoproduction no significant suppression is found in photoproduction. This was previously reported in [35].

8 Summary

Diffractive dijet production has been measured in the same kinematic regions for DIS and photoproduction using the same jet algorithm to allow the closest possible comparison of the cross sections. Next-to-leading order QCD calculations for the production of dijets have been interfaced with diffractive parton distributions determined by H1 from inclusive diffractive DIS data to test QCD factorisation in diffraction.

The NLO prediction in DIS describes the measured distributions reasonably well within the theoretical and experimental uncertainties. The concept of QCD factorisation is compatible with the measurement results in diffractive DIS. In photoproduction, the NLO calculation overestimates the dijet rate significantly but describes the shapes of the measured distributions well within the theoretical and experimental uncertainties. The data strongly favour a suppression of both the resolved and the direct component of the NLO calculation in photoproduction by about the same factor ≈ 0.5 over a model which suppresses only that part of the calculation for which at the parton level $x_\gamma^{\rm jets} < 0.9$ by a factor 0.34. This disfavours models which describe the breaking of factorisation as the effect of secondary interactions among spectator partons.

The ratio of data to NLO prediction in photoproduction is a factor 0.5 ± 0.1 (exp.) smaller than the same ratio in DIS. This shows a breaking of QCD factorisation in diffractive dijet photoproduction with respect to the same process in DIS.

Acknowledgements

We are grateful to the HERA machine group whose outstanding efforts have made and continue to make this experiment possible. We thank the engineers and technicians for their work in constructing and now maintaining the H1 detector, our funding agencies for financial support, the DESY technical staff for continual assistance, and the DESY directorate for the hospitality which they extend to the non-DESY members of the collaboration.

References

[1] J. Collins, Phys. Rev. **D57** (1998) 3051 and erratum ibid. **D61** (2000) 019902.

[2] H1 Collaboration, C. Adloff *et al.*, Z. Phys. **C76** (1997) 613.

[3] H1 Collaboration, paper 980 submitted to 31st Intl. Conf. on High Energy Physics, ICHEP 2002, Amsterdam.

[4] H1 Collaboration, paper 113 submitted to Intl. Europhysics Conference on High Energy Physics, EPS 2003, Aachen.

[5] CDF Collaboration, T. Affolder *et al.*, Phys. Rev. Lett. **84** (2000) 5043.

[6] E. Gotsman, E. Levin, U. Maor, Phys. Lett. **B438** (1998) 229;
B. Cox, J. Forshaw, L. Lönnblad, [hep-ph/9908464];
A. Kaidalov, V. Khoze, A. Martin, M. Ryskin, [hep-ph/0306134].

[7] H1 Collaboration, C. Adloff *et al.*, Eur. Phys. J. **C6** (1999) 421.

[8] L. Trentadue, G. Veneziano, Phys. Lett. **B323** (1994) 201;
A. Berera, D. Soper, Phys. Rev. **D50** (1994) 4328;
M. Grazzini, L. Trentadue, G. Veneziano, Nucl. Phys. **B519** (1998) 394.

[9] W. Buchmüller, T. Gehrmann, A. Hebecker, Nucl. Phys. **B537** (1999) 477.

[10] F. Hautmann, Z. Kunszt, D. E. Soper, Nucl. Phys. **B563** (1999) 153;
F. Hautmann, D. E. Soper, Phys. Rev. **D63** (2000) 011501.

[11] L. Alvero, J. C. Collins, J. Terron, J. J. Whitmore, Phys. Rev. **D59** (1999) 074022.

[12] C. Royon, L. Schoeffel, J. Bartels, H. Jung, R. Peschanski, Phys. Rev. **D63** (2001) 074004.

[13] G. Ingelman, P. Schlein, Phys. Lett. **B152** (1985) 256.

[14] H1 Collaboration, C. Adloff *et al.*, Eur. Phys. J. **C20** (2001) 29.

[15] H. Jung, Comp. Phys. Commun. **86** (1995) 147.

[16] M. Glück, E. Reya, A. Vogt, Phys. Rev. **D46** (1992) 1973;
M. Glück, E. Reya, A. Vogt, Phys. Rev. **D45** (1992) 3986.

[17] H1 Collaboration, C. Adloff *et al.*, Phys. Lett. **B483** (2000) 36.

[18] G. Schuler, T. Sjöstrand, Phys. Lett. **B376** (1996) 193.

[19] H1 Collaboration, C. Adloff *et al.*, Eur. Phys. J. **C13** (2000) 397.

[20] M. Bengtsson, T. Sjöstrand, Z. Phys. **C37** (1988) 465.

[21] T. Sjöstrand, Comp. Phys. Commun. **39** (1986) 347;
T. Sjöstrand, M. Bengtsson, Comp. Phys. Commun. **43** (1987) 367.

[22] A. Kwiatkowski, H. Spiesberger, H. Möhring, Comp. Phys. Commun. **69** (1992) 155.

[23] T. Sjöstrand *et al.*, Comp. Phys. Commun. **135** (2001) 238.

[24] S. Catani, M. H. Seymour, Nucl. Phys. **B485** (1997) 29 [erratum-ibid. **B510** (1997) 503].

[25] F. Hautmann, JHEP **0210** (2002) 025.

[26] C. Duprel, T. Hadig, N. Kauer, M. Wobisch, "Comparison of next-to-leading order calculations for jet cross-sections in deep inelastic scattering" in A. Doyle, G. Grindhammer, G. Ingelman, H. Jung (eds.), Proc. of the Workshop on Monte Carlo Generators for HERA Physics, DESY-PROC-1999-02 (1999).

[27] S. Frixione, Z. Kunszt and A. Signer, Nucl. Phys. **B467** (1996) 399;
S. Frixione, Nucl. Phys. **B507** (1997) 295;
see also http://www.ge.infn.it/∼ridolfi/.

[28] H1 Collaboration, I. Abt *et al.*, Nucl. Instrum. Methods **A386** (1997) 310 and 348.

[29] H1 SpaCal Group, T. Nicholls *et al.*, Nucl. Instrum. Methods **A374** (1996) 149;
H1 SpaCal Group, T. Nicholls *et al.*, Nucl. Instrum. Methods **A386** (1997) 397.

[30] S. Ellis, D. Soper, Phys. Rev. **D48** (1993) 3160;
S. Catani, Y. Dokshitzer, M. Seymour, B. Webber, Nucl. Phys. **B406** (1993) 187.

[31] H1 Collaboration, C. Adloff *et al.*, Z. Phys. **C74** (1997) 221.

[32] B. List, Diploma Thesis, Techn. Univ. Berlin, Germany, (1993), unpublished;
B. List, A. Mastroberardino, *DIFFVM: A Monte Carlo Generator for diffractive processes in ep scattering* in *Monte Carlo Generators for HERA Physics*, A. Doyle, G. Grindhammer, G. Ingelman, H. Jung (eds.), DESY-PROC-1999-02 (1999) 396.

[33] H1 Collaboration, paper 5-0165 submitted to 32nd Intl. Conf. on High Energy Physics, ICHEP 2004, Beijing.

[34] A. Kaidalov, V. Khoze, A. Martin, M. Ryskin, Phys. Lett. **B567** (2003) 61.

[35] H1 Collaboration, paper 087 submitted to Intl. Europhysics Conf. on High Energy Physics, EPS 2003, Aachen.

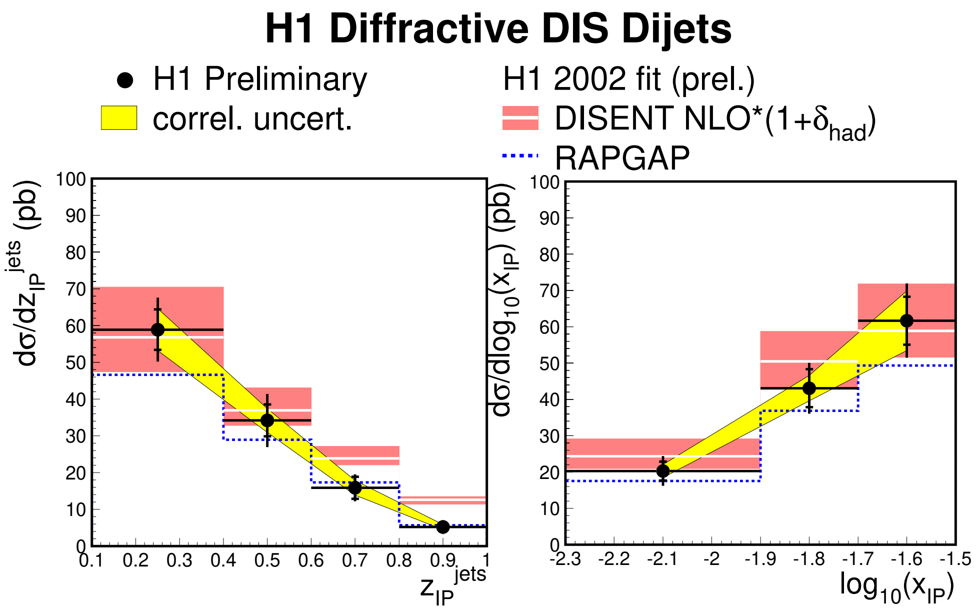

(a) (b)

Figure 4: Cross section for the diffractive production of two jets in the DIS kinematic region specified in Table 1 as a function of a) $z_{I\!P}^{\rm jets}$ and b) $\log_{10}(x_{I\!P})$. Also shown is the NLO prediction of the DISENT program interfaced to the 'H1 2002 fit' diffractive NLO PDFs and the RAPGAP prediction which contains parton showers and is based on the LO PDFs from the same fit. Both predictions include models of hadronisation effects. The inner error bars represent the statistical errors and the outer error bars the quadratic sum of the statistical and uncorrelated systematic errors. The shaded band around the data points shows correlated normalisation uncertainties. The band around the NLO prediction indicates the uncertainty resulting from the variation of the renormalisation scale by factors 0.5 and 2. Not shown is the uncertainty resulting from the uncertainty on the diffractive parton densities and the uncertainty due to the imperfect knowledge of the hadronisation corrections.

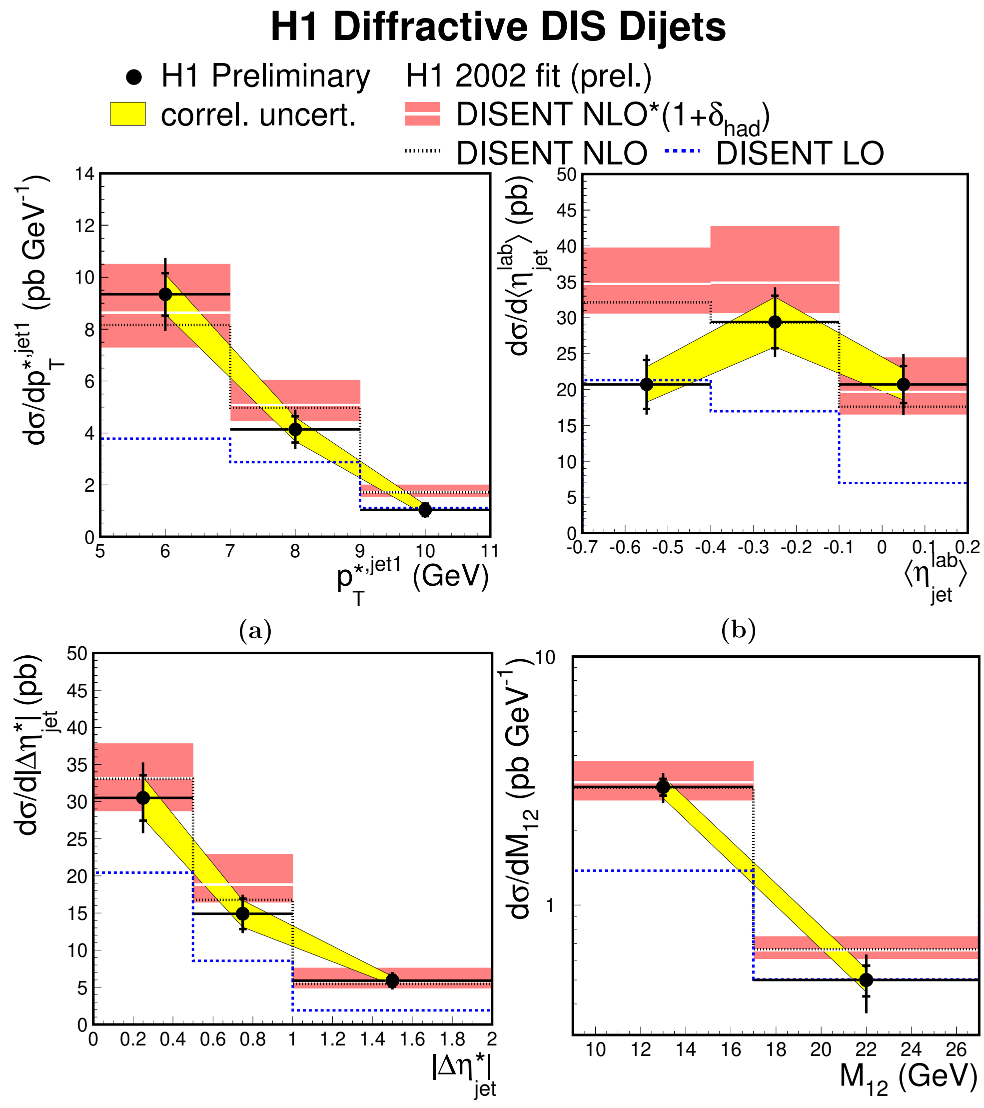

Figure 5: Cross section for the diffractive production of two jets in the DIS kinematic region specified in Table 1 as a function of the jet variables a) $p_T^{*,\mathrm{jet1}}$, b) $\langle\eta_{\mathrm{jet}}^{\mathrm{lab}}\rangle$, c) $\left|\Delta\eta_{\mathrm{jet}}^{*}\right|$ and d) M_{12}. Also shown is the DISENT prediction based on the 'H1 2002 fit' diffractive PDFs at NLO with and without hadronisation corrections and at LO without hadronisation corrections. For details see the caption of Figure 4.

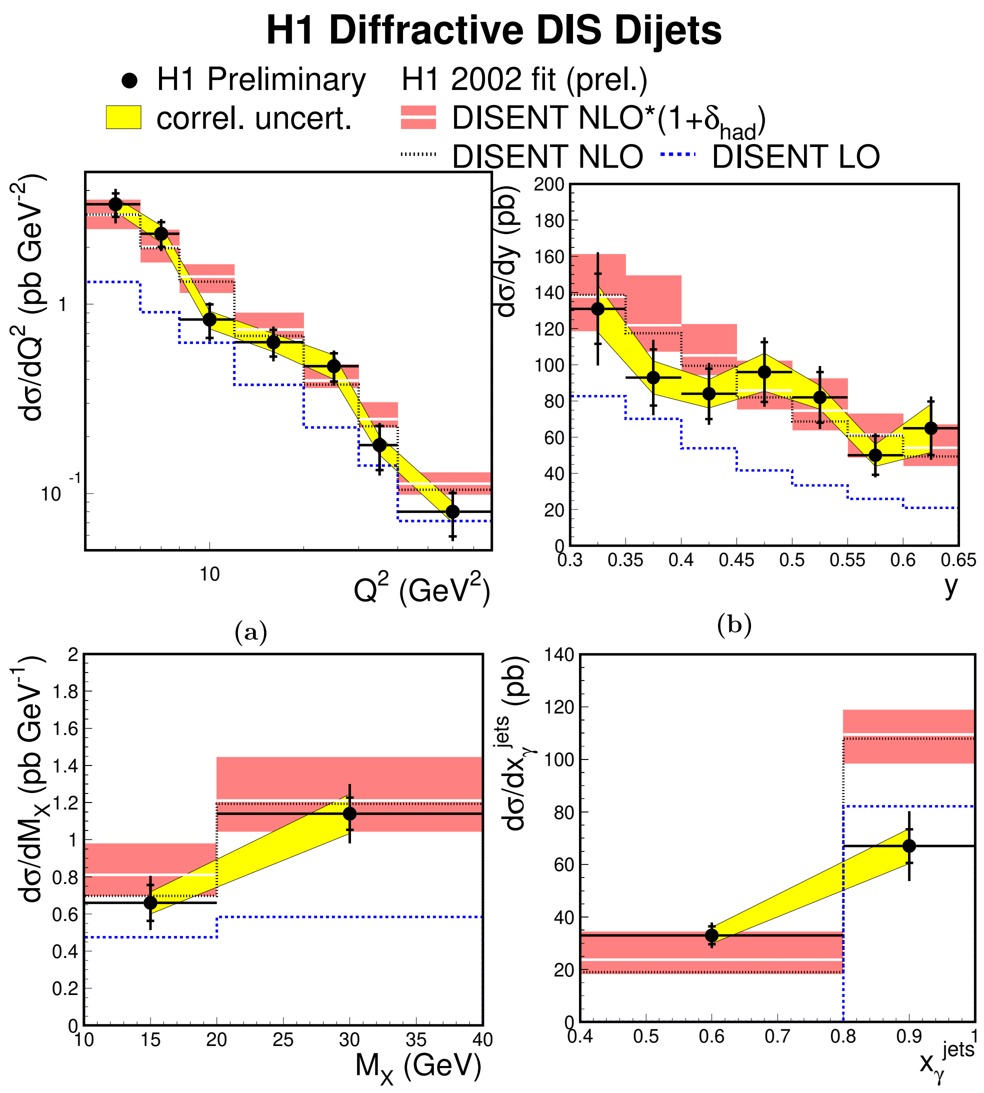

(a) (b) (c) (d)

Figure 6: Cross section for the diffractive production of two jets in the DIS kinematic region specified in Table 1 as a function of the variables a) Q^2, b) y, c) M_X and d) $x_\gamma^{\rm jets}$. Also shown is the DISENT prediction based on the 'H1 2002 fit' diffractive PDFs at NLO with and without hadronisation corrections and at LO without hadronisation corrections. For details see the caption of Figure 4.

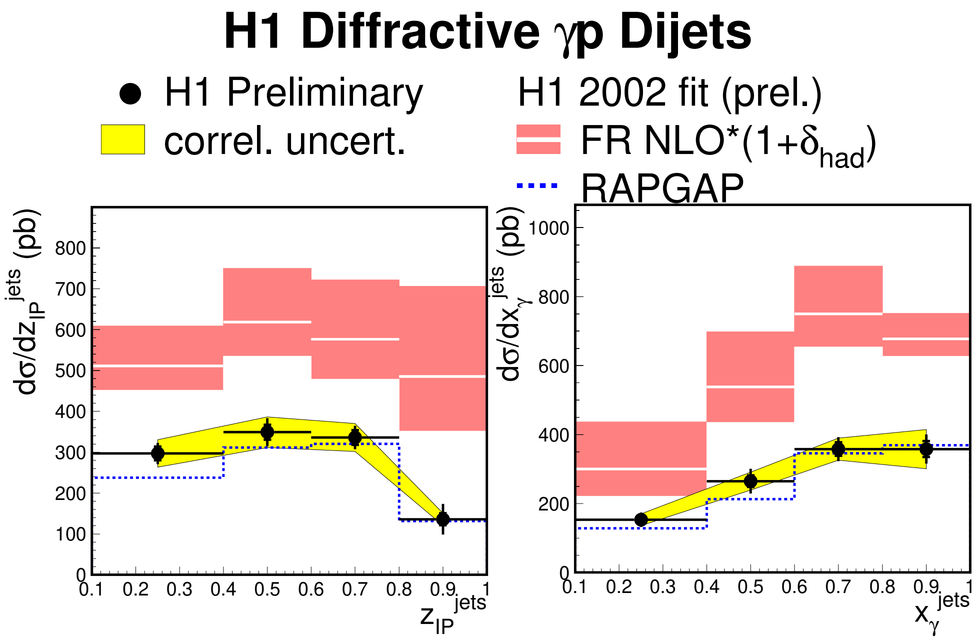

(a)

(b)

Figure 7: Cross section for the diffractive production of two jets in the photoproduction kinematic region specified in Table 1 as a function of a) $z_{I\!P}^{\rm jets}$ and b) $x_\gamma^{\rm jets}$. Also shown is the NLO prediction of the Frixione et al. program interfaced to the 'H1 2002 fit' diffractive NLO PDFs and the RAPGAP prediction, which contains parton showers and is based on the LO PDFs from the same fit. Both predictions include the effects of hadronisation. The inner error bars represent the statistical errors and the outer error bars the quadratic sum of the statistical and uncorrelated systematic errors. The shaded band around the data points shows correlated normalisation uncertainties. The band around the NLO prediction indicates the uncertainty resulting from simultaneous variations of the renormalisation and factorisation scales by factors 0.5 and 2. Not shown is the uncertainty resulting from the uncertainty on the diffractive parton densities and the uncertainty due to the imperfect knowledge of the hadronisation corrections.

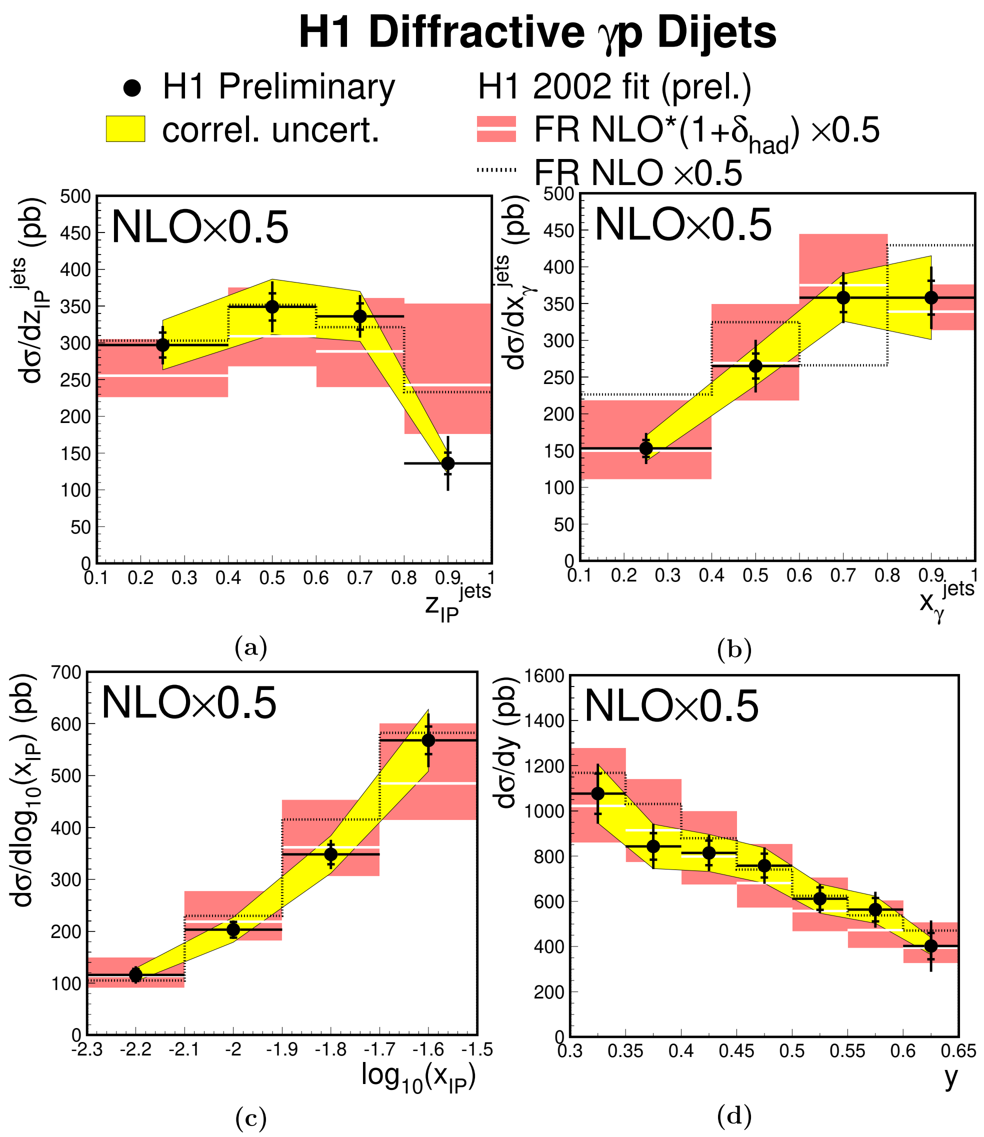

(a) (b) (c) (d)

Figure 8: Cross section for the diffractive production of two jets in the photoproduction kinematic region specified in Table 1 as a function of a) $z_{I\!P}^{\rm jets}$, b) $x_\gamma^{\rm jets}$, c) $\log_{10}(x_{I\!P})$ and d) y. Also shown is the NLO prediction of the Frixione et al. program interfaced to the 'H1 2002 fit' diffractive PDFs with and without hadronisation corrections, scaled by an overall normalisation factor 0.5. For details see the caption of Figure 7.

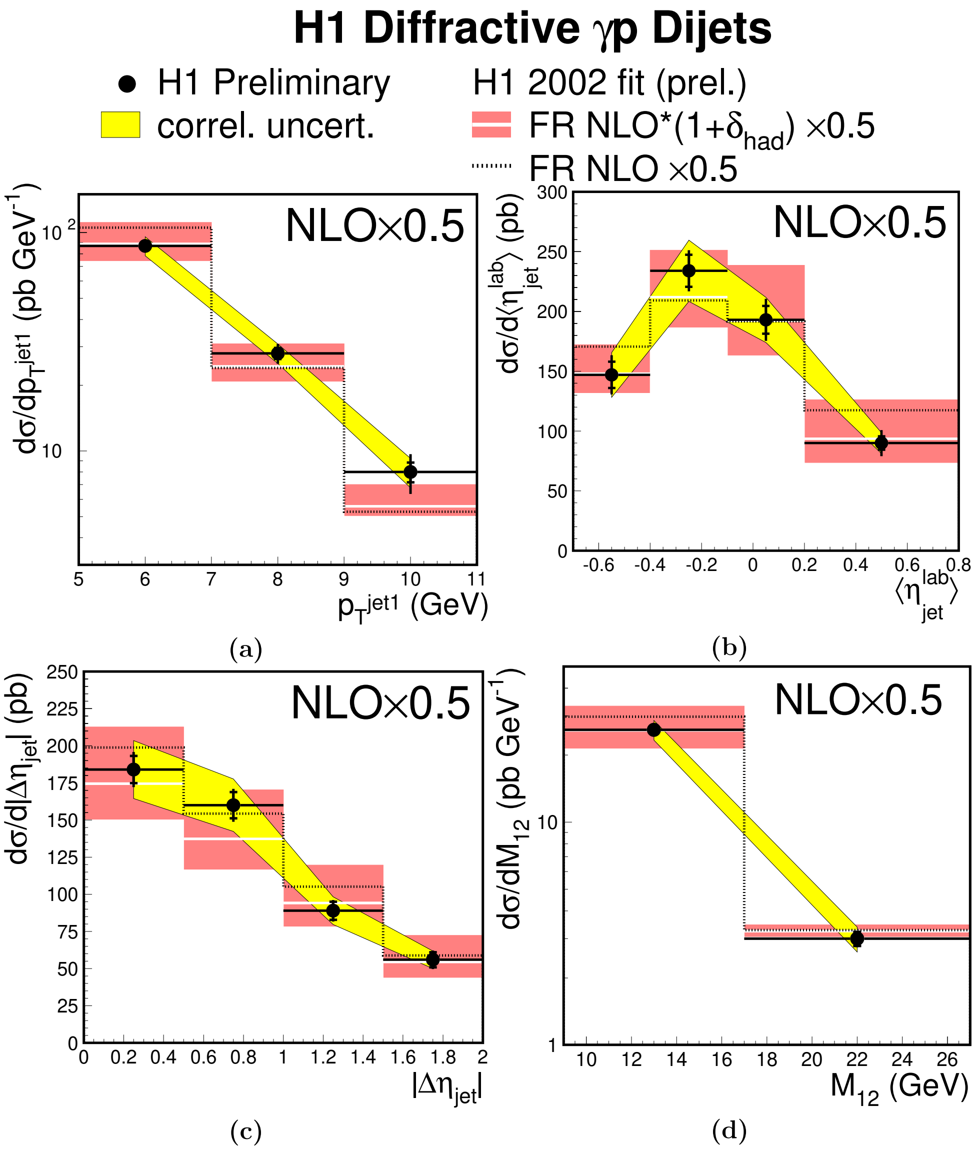

Figure 9: Cross section for the diffractive production of two jets in the photoproduction kinematic region specified in Table 1 as a function of the jet variables a) p_T^{jet1}, b) $\langle\eta_{\mathrm{jet}}^{\mathrm{lab}}\rangle$, c) $|\Delta\eta_{\mathrm{jet}}|$ and d) M_{12}. Also shown is the NLO prediction of the Frixione et al. program interfaced to the 'H1 2002 fit' diffractive PDFs with and without hadronisation corrections, scaled by an overall normalisation factor 0.5. For details see the caption of Figure 7.

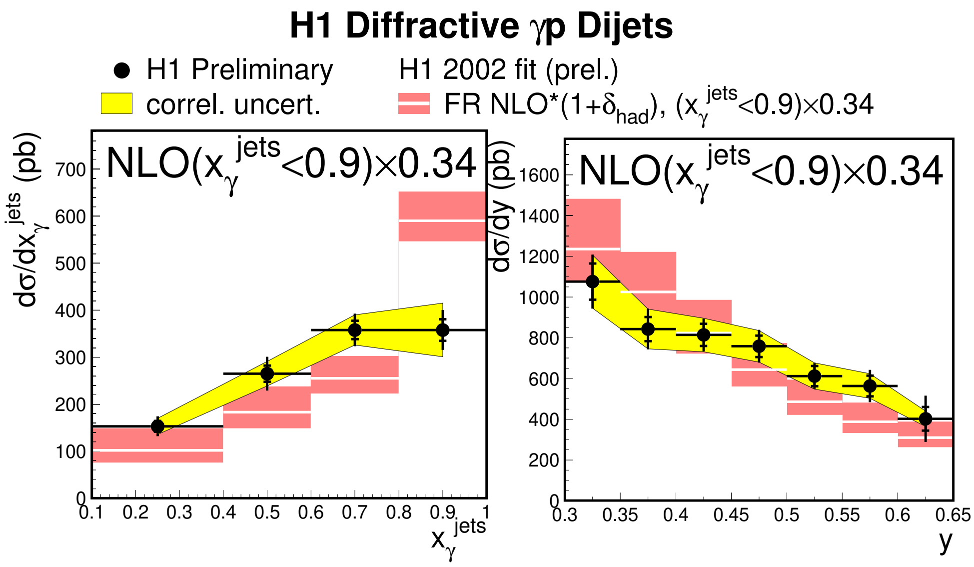

(a) (b)

Figure 10: Cross section for the diffractive production of two jets in the photoproduction kinematic region specified in Table 1 as a function of a) $x_\gamma^{\rm jets}$ and b) y. Also shown is the NLO prediction of the Frixione et al. program interfaced to the 'H1 2002 fit' diffractive PDFs with hadronisation corrections. The part of the NLO calculation for which at the parton level $x_\gamma^{\rm jets} < 0.9$ is scaled by 0.34. For details see the caption of Figure 7.

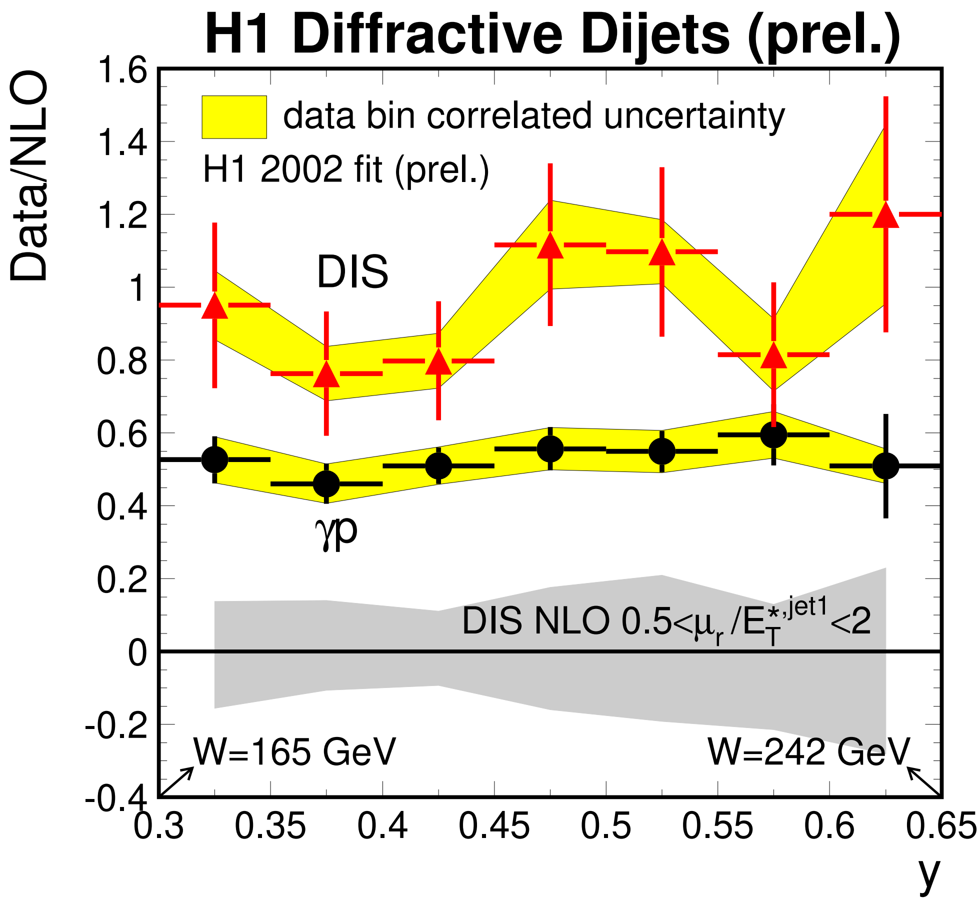

Figure 11: Ratio of data to NLO prediction for the diffractive production of two jets in the photoproduction and DIS kinematic regions specified in Table 1 as a function of y. The vertical error bars indicate the uncorrelated experimental uncertainty. The error band around the ratio points shows an additional experimental normalisation uncertainty. The NLO predictions are based on the 'H1 2002 fit' diffractive PDFs and are corrected for hadronisation effects. The uncertainty arising from the variation of the renormalisation scale in the DIS NLO calculation is shown at the bottom and is fully correlated between bins. The range shown in y corresponds to a range $165 < W < 242$ GeV in the γp centre-of-mass energy.